THE STAR FORMATION NEWSLETTER

No. 334 1-7

2020. 12. 4　泉奈都子（ASIAA）

1. Gravitoviscous Protoplanetary Disks with a Dust Component. IV. Disc Outer Edges, Spectral Indices, and Opacity Gaps

2. Hints for icy pebble migration feeding an oxygen-rich chemistry in the inner planet-forming region of disks

3. Gravity and rotation drag the magnetic field in high-mass star formation

4. Observations of the Onset of Complex Organic Molecule Formation in Interstellar Ices

5. SiO emission as a probe of Cloud-Cloud Collisions in Infrared Dark Clouds

6. Chemical evolution during the formation of Protoplanetary Disk

7. Time-Variable Radio Recombination Line Emission in W49A

2. Hints for icy pebble migration feeding an oxygen-rich chemistry in the inner planet-forming region of disks

Andrea Banzatti et al. Accepted by ApJ https://arxiv.org/pdf/2009.13525

Outer diskの半径とinner diskに存在する分子量を比較して, disk進化と惑星形成の関係を明らかにする

- 先行研究: Najita et al. (2013)
  - HCN/H_2O flux ratioとdust disk massに正の相関を発見
    - 分子輝線: 星から数au以内のガスをトレース
    - Dust disk mass: outer disk（> 20au）内のdust grainをトレース

      → H_2O iceはsnow lineより外側の微惑星や核に閉じ込められ, inner disk ではC/Oが増加することの証拠であり, さらにこの現象はより大きいdiskにおいて顕著に起こることを示唆

      → Inner disk内の分子がouter diskで起こる微惑星形成における”chemical finger print”となることを示唆

      → 本論文: Najita et al. (2013) の研究をより発展させる
      - 3倍以上の数のサンプル
      - H_2O, HCN, C_2H_2, CO_2について調べる
      - 不定性の問題をなくすため, 質量の代わりにdiskの半径を用いる

- サンプルと使用データ
  - サンプル　　: 63個のpre-main-sequence star周りのprotoplanetary disk
    - 近傍(< 200 pc) にあるT Tauri stars (年齢は 1-3 Myr)
    - 半径は~10auから>200 auまで網羅
    - full diskのものとinner cavityを持つものがある
  - Dust diskの半径: ALMA, SMAの高解像度のサーベイデータ
  - 分子ガス輝線　: Spitzerのスペクトルデータ

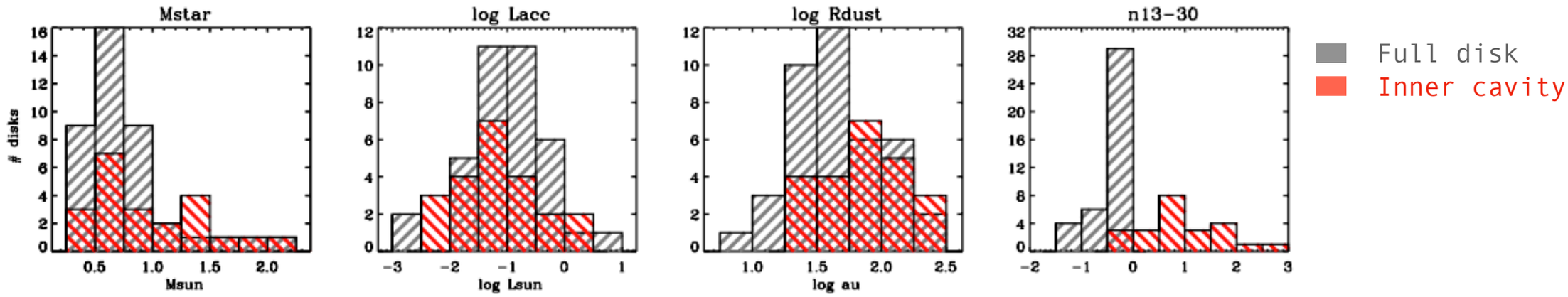

Figure 1. Sample property distributions (see Section 2 for details). Full disks are shown in grey; disks with inner cavities are shown in red.

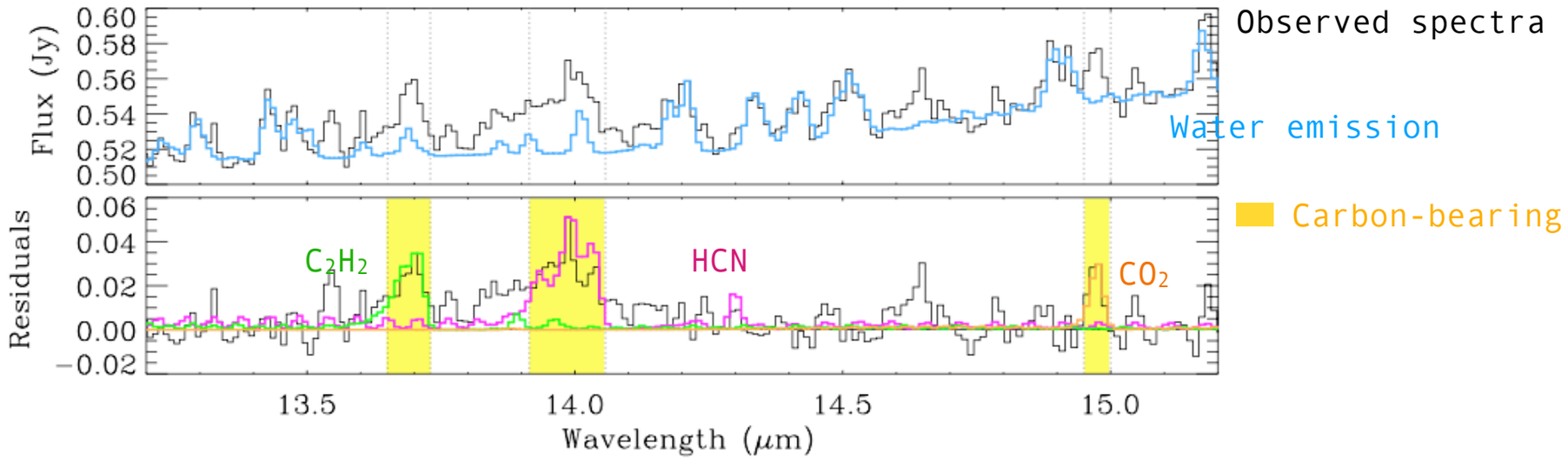

Figure 2. Correction of carbon-bearing molecular features from water contamination in *Spitzer*-IRS spectra. The spectrum of CI Tau is shown as an example. *Top*: observed spectrum in black, water emission model in cyan (see Section 2.3). *Bottom*: residuals after subtraction of the water emission model from the data. Models of carbon-bearing molecular emission features are shown for guidance (but are not fits to the data): C_2H_2 at 13.7 μm in green, HCN at 14 μm in magenta, CO_2 at 14.95 μm in orange. The yellow shaded area indicates the ranges where carbon-bearing molecular line fluxes are measured.

- Results
  - H_2O/HCN, H_2O/C_2H_2, H_2O/CO_2 の全てにおいて半径との負の相関が見られた

    ↑ Accretion luminosityの影響を除くと（正規化）, H_2Oのみ半径との相関が見られた

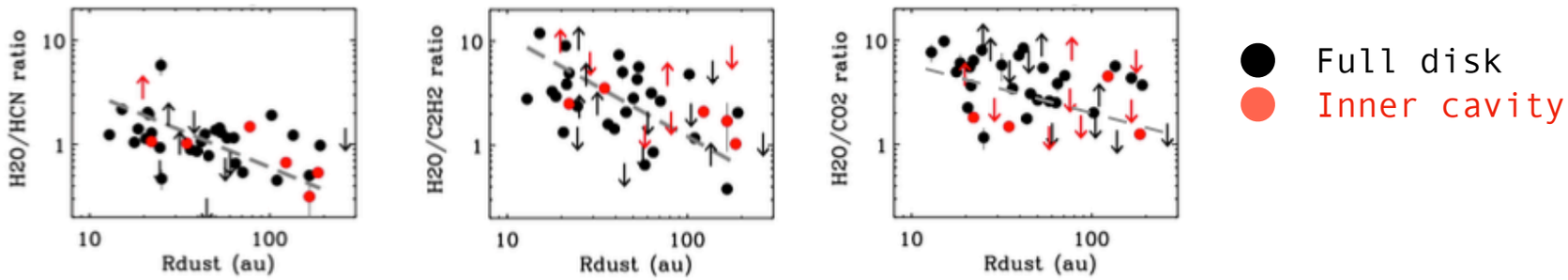

Figure 4. Correlations between water/carbon-bearing-molecules line flux ratios and millimeter disk radii (see Section 2 for details). Red datapoints identify disks that have an inner dust cavity. Linear regression fits are shown with dashed lines.

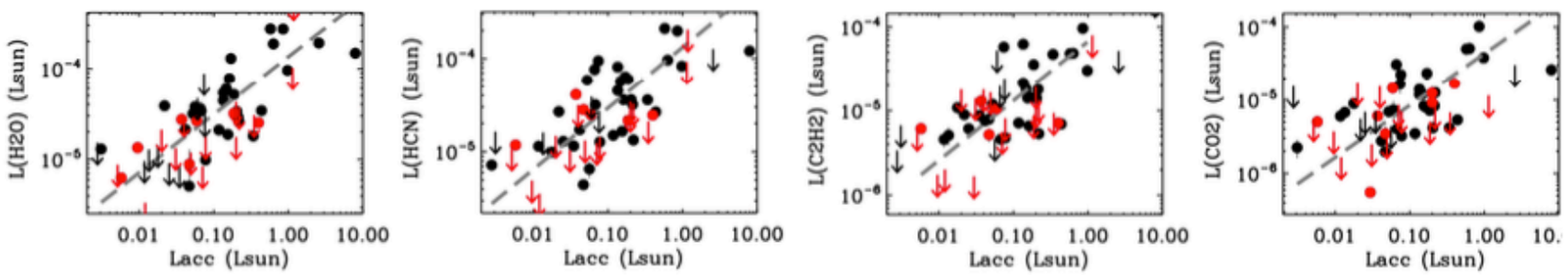

Figure 5. Correlations between molecular line luminosity and accretion luminosity. Linear regression fits are shown with dashed lines. All fits are consistent with a power law of index 0.6 (Table 1), as $L_{\rm molecule} \propto L_{\rm acc}^{0.6}$.

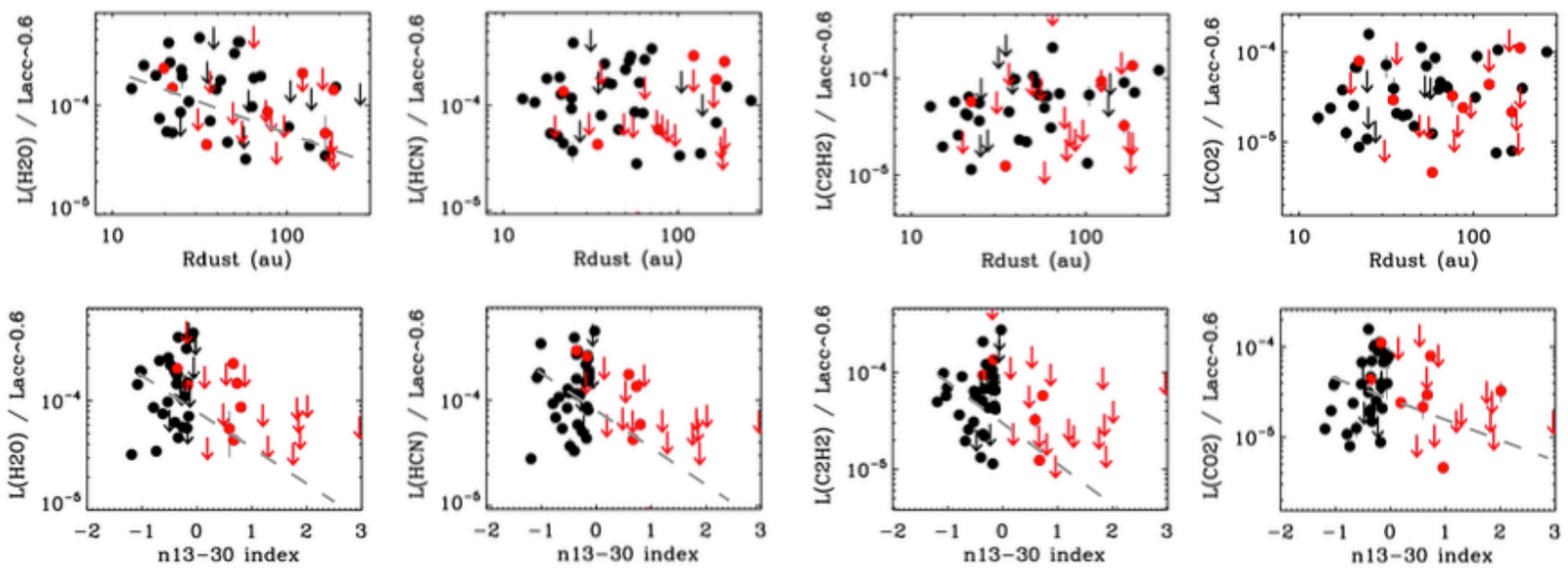

Figure 6. Correlations between molecular luminosity divided by $L_{\rm acc}^{0.6}$ and disk radius (top) or infrared index (bottom). Linear regression fits are shown with dashed lines where a correlation is detected in the data.

- Results
  - Inner disk領域は外側から移動してきたoxygen-rich icy pebbleが昇華することでwater vapor enrichmentになる

    → Inner diskのchemistryはouter diskの進化と関係している！

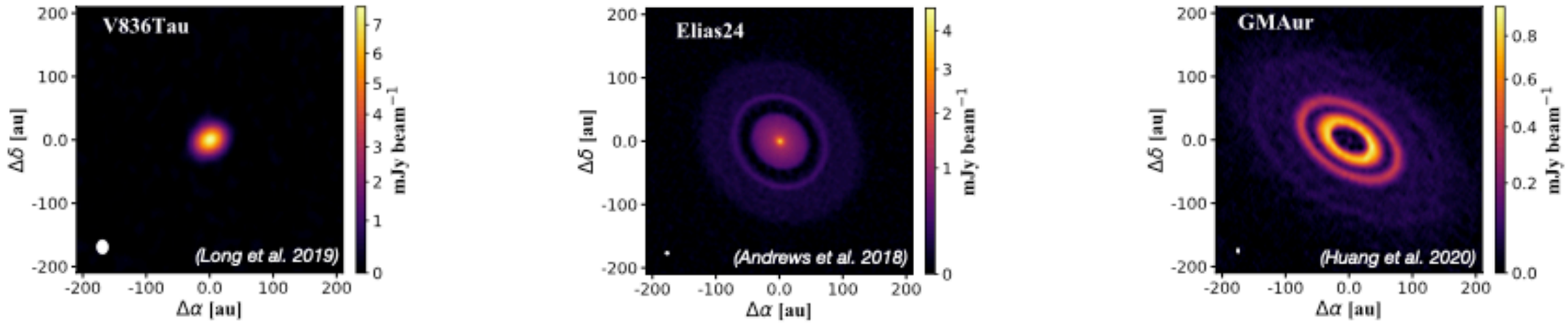

Figure 7. Cartoon to visualize our interpretation of the results from this analysis. Efficient drift of icy pebbles in small disks leads to large columns of water vapor inside the snow line, and therefore to a high infrared H_2O luminosity (Section 3). Large disks have substructures where icy pebbles are trapped in the outer disk, lowering the columns of inner water vapor and decreasing the H_2O luminosity. Similar or lower columns are found in disks with an inner cavity, where dust and gas are depleted. Indicative column density values for the three size-bins of disk radii are taken from fits to water emission in *Spitzer* spectra (Salyk et al. 2011a, and Appendix E). The images to the top show representative disks from Long et al. (2019) for small disks, Andrews et al. (2018b) for large disks with substructures, and Huang et al. (2020) for large disks with a cavity.

3. Gravity and rotation drag the magnetic field in high-mass star formation

S. Feng et al. Accepted by ApJ https://www2.mpia-hd.mpg.de/homes/beuther/beuther2020b.pdf

大質量星形成領域内部のダイナミクスにおいて、重力/回転/磁場のどれが支配的？

- Observation
  - Target: massive hot core G327.3
    - D ~ 3.1 kpc
    - Luminosity ~ 10^5 $L_\odot$
    - Mass ~ 950$M_\odot$
    - CH_3OH class II maser emission
    - Line-rich star-forming hot molecular core (T > 100 K)
  - Telescope: ALMA
    - 1.3 mm band (230.852, 229.152, 216.442, 214.535 GHz)

- Simulation
  - MHD code: Pluto
  - Gravitational collapse of a magnetized pre-stelar core
    - Mass: 100 $M_\odot$
    - Gas and dust within a sphere in 0.1 pc (radius)
    - Radial slope of the gas mass density: $r^{-1.5}$
    - Core: solid-body rotation with about 4 % or rotational to gravitational energy
    - Initial temperature: 10 K

- Result

Figure 1. Compilation of the G327.3 continuum and dense gas emission data. The left and central panels present in color the 1.3 mm continuum Stokes I and linearly polarized P emission, respectively. The contours start at the 3σ levels continuing in 6σ steps up to 42σ, then increasing further in 84σ steps (1σ are 1.5 mJy beam^{-1} and 50 μJy beam^{-1} for Stokes I and linearly polarized emission, respectively). The central core (C) and two positions toward the north-east (NE1 & NE2) are marked. The box in the middle panel shows the zoom-region presented in the right panel. There, the color-scale presents the 1st moment (intensity-weighted peak velocity) of $^{13}CH_3CN(12_4 - 11_4)$. The constant-length line segments show in all three panels the magnetic field orientation (polarization angles rotated by 90 deg) derived from the linearly polarized continuum data above the 2σ level (independent of the polarization fraction). Linear scale bars are presented in the left and right panels, the synthesized beam ($1.16'' \times 0.96''$) is shown in all panels in the bottom-left corner. The green circle in the right panel outlines the $2''$ radius aperture where rotation appears to distort the magnetic field (see also section 4.2.1).

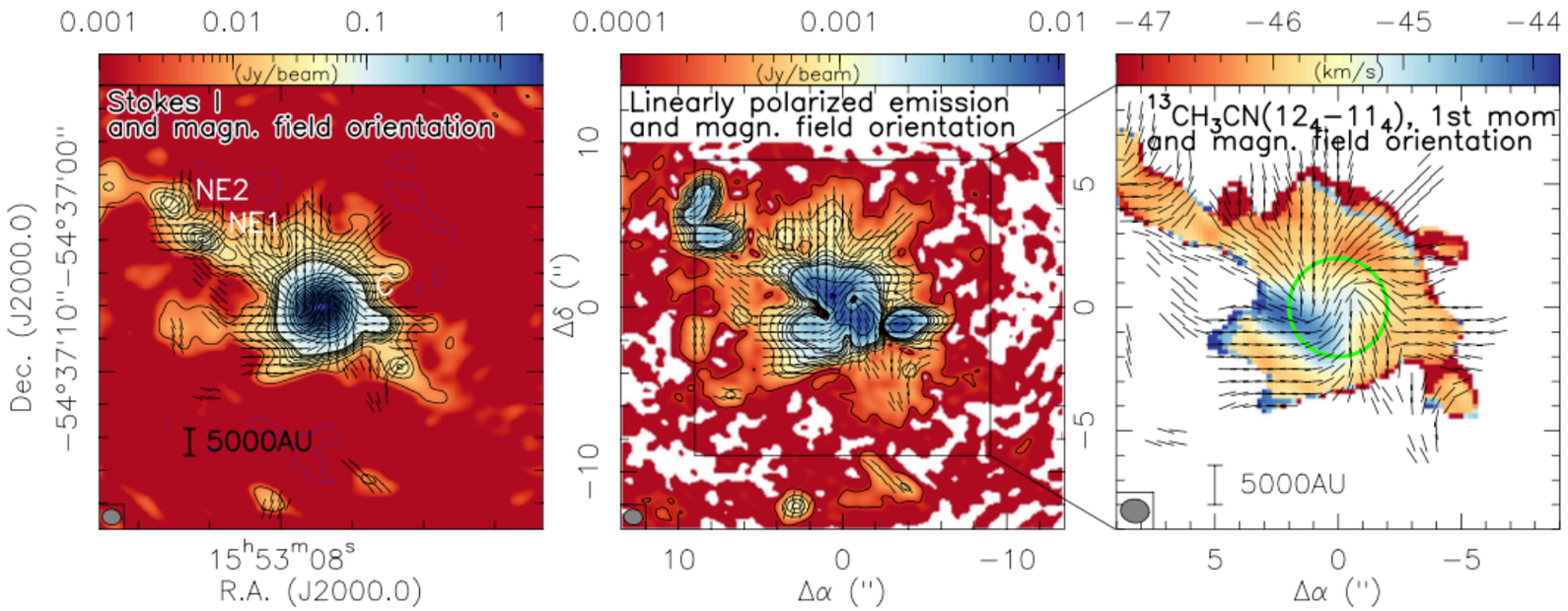

Table 1. Stokes I continuum parameters

Source	S (Jy)	S_{peak} (Jy beam^{-1})	M ($M_\odot$)	N (10^{24}cm^{-2})
C	9.81	1.966	435^{+485}_{-223}	$13.4^{+15.0}_{-6.9}$
NE1	0.065	0.046	$9.2^{+10.3}_{-4.7}$	$0.4^{+0.5}_{-0.2}$
NE2	0.035	0.031	$4.0^{+4.4}_{-2.1}$	$0.2^{+0.3}_{-0.1}$

Notes: Sources are labeled in Fig. 1. Flux densities S, peak intensities S_{peak}, masses M and gas column densities N are given. The error margins for M and N correspond to an uncertainty of a factor 2 in the temperature.

- ダスト連続波は中心にあるコア以外にフィラメント構造
  （Polarized emissionの構造も似ている）
- 磁場構造はピーク値から放射状に分布している
- フィラメント構造(NE1, NE2)において磁場はU字型構造をしている

→ 磁場は重力によってコアの中心部に引っ張られていることを示す

- $^{13}CH_3CN$の速度構造はコアの回転を示唆 ← 磁場は回転に沿った構造をしている
- CO(2-1)の構造により(論文内に図なし), この天体はface-onである可能性が高い

- Result

  - シミュレーション結果は観測結果と似ている

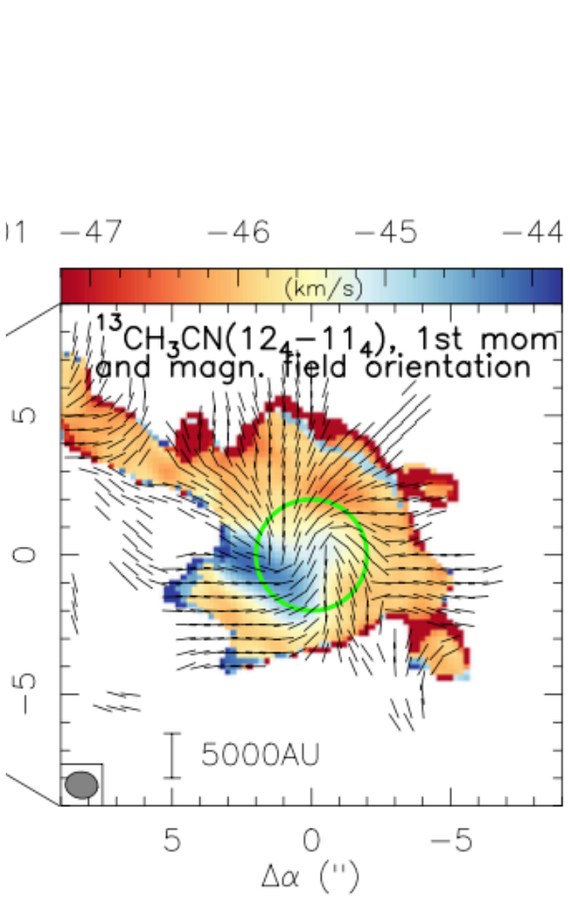

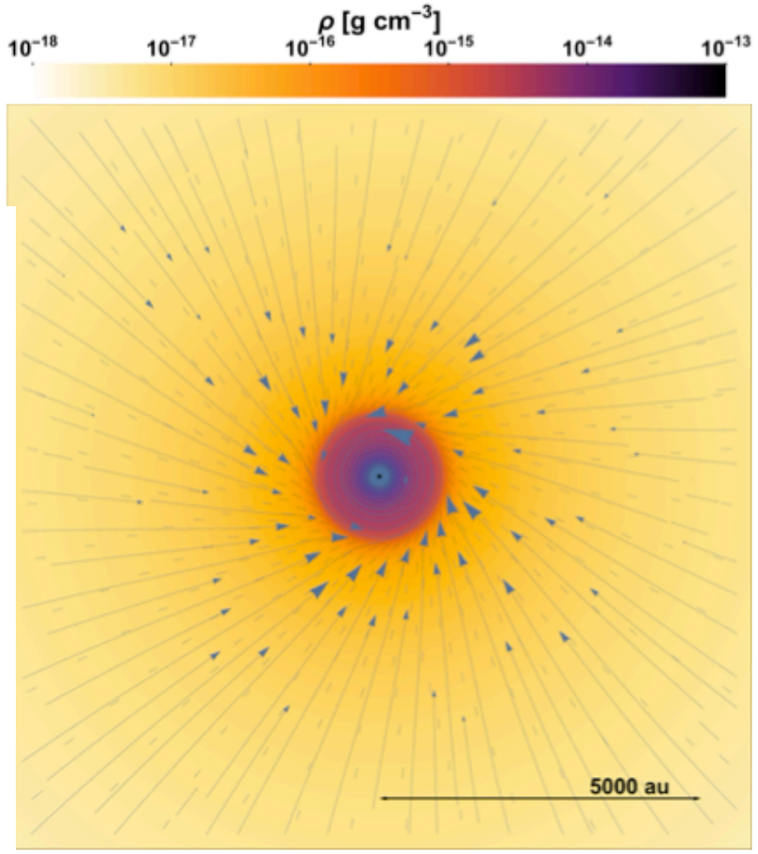

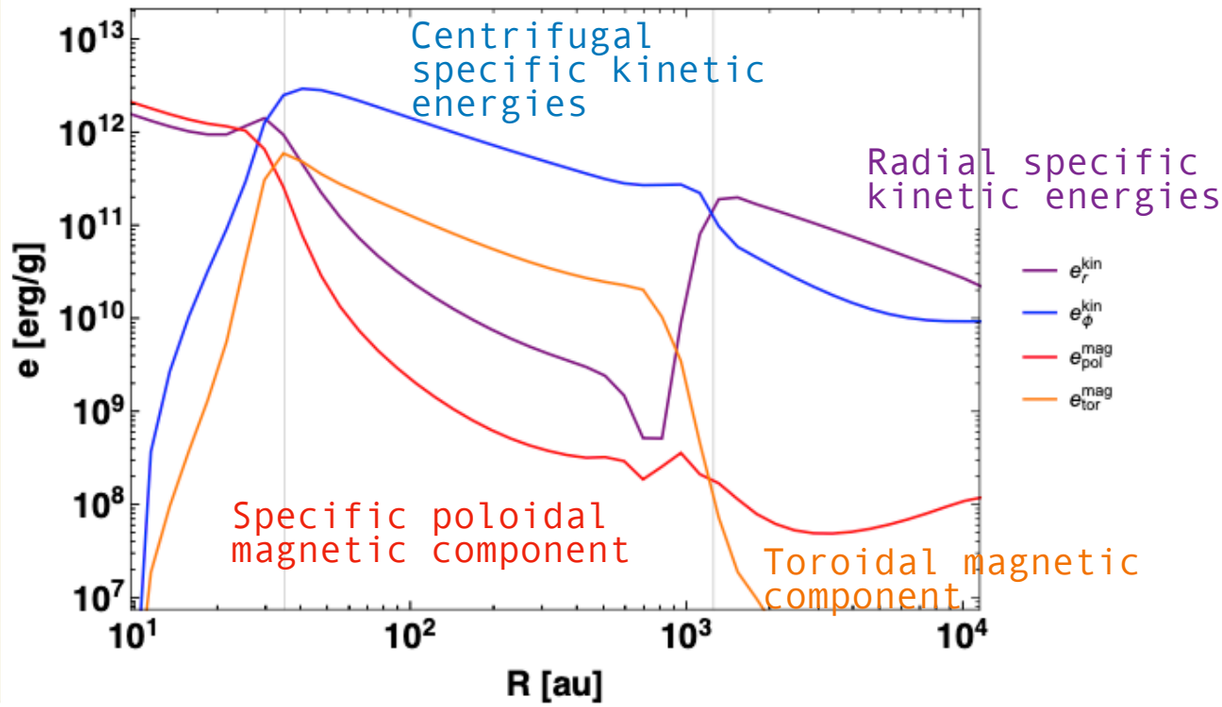

Figure 4. Numerical cloud collapse model. Face-on view of the gas mass density distribution (color) and magnetic field morphology (segments and arrows) in the midplane. The left image shows a zoom onto the central region at 30 kyr after onset of the gravitational collapse. Blue line segments represent local magnetic field orientation, the arrows connect them to trajectories/field lines. Details are given in Sec. 3. The right panel presents the radially averaged energy profiles for the radial/azimuthal specific kinetic energies (e_r^{kin}, e_ϕ^{kin}) and the poloidal/toroidal specific magnetic energies ($e_{pol}^{mag}, e_{tor}^{mag}$), respectively. The vertical lines at 35 and 1250 AU mark approximate transition regions.

  - この領域では, 重力と回転がダイナミクスを支配し, 磁場の形態を形作っている

5. SiO emission as a probe of Cloud-Cloud Collisions in Infrared Dark Clouds

G. Consentino et al. Accepted by MNRAS https://arxiv.org/pdf/2009.13890

最終目的: Infrared Dark Cloudsとその内部の形成メカニズムを解明

- Infrared Dark Clouds (IRDCs)
  - 高密度 ($n(H_2) \sim 10^3$-10^4 cm^{-3}) かつ低温度 ($T \leqq 25$ K) の領域であり, 大質量形成初期段階であると考えられている
  - その形成メカニズムは未だ解明されていないが, **“既存のより大きな分子雲and/or フィラメント間における低速衝突 (~ 10 km/s) によって形成される”**と示唆されている

→ 速度幅が小さく, かつ広がったショックトレーサー（e.g. SiO）の輝線が検出されるはず…

IRDCの例

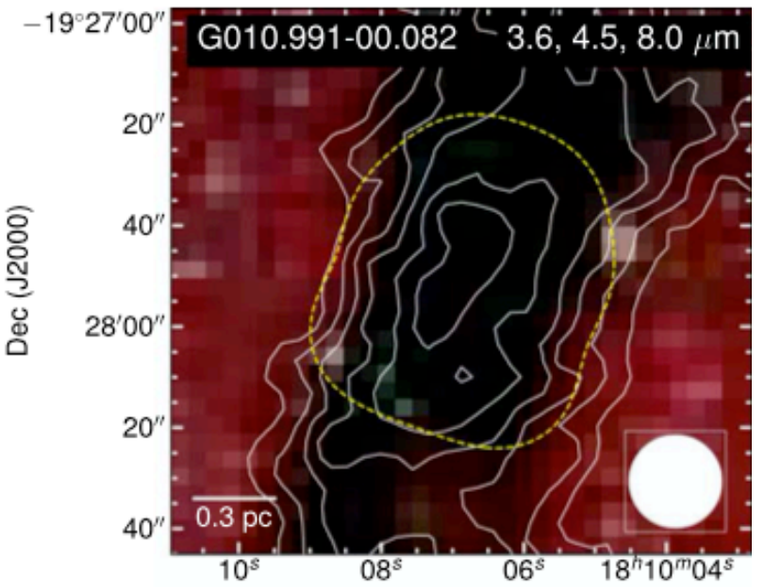

Sanhueza et al.2019

（Jimenez-Serra et al. (2002) 等の複数の先行研究で既に検出が報告されている）

→ 本論文：IRDCにおけるSiOの空間分布とkinematic structureを調べてCloud-Cloud collisionの兆候を探る

- Observation
  - ターゲット: 比較的近くにあり(≦ 6 kpc) 質量の重い (0.2-29 × 10^3 M_{sun}) 6つのIRDC
  - 望遠鏡：IRAM30m
  - 輝線　：SiO(2-1)
  - 空間分解能：30”
  - 速度分解能：0.16 km/s

Table 1. Names, central coordinates, velocities with respect to the Local standard rest (V_{LSR}), kinematic distances, effective radii and masses of the six IRDCs. For each cloud, the offset position, map size and achieved rms are also reported.

Cloud	Central Coordinates[a]		V^b_{LSR}	d[b]	R^c_{eff}	Mass[d]	Off Position	Map Size	rms
	RA(J2000)	DEC(J2000)	[km s^{-1}]	[kpc]	[pc]	[10^3 $M_\odot$]	[″,″]	[″×″]	[mK]
(A) G018.82−00.28	18:26:18.7	-12:41:16.3	65.8	4.8	10.4	18.5	−200,+100	300×240	5
(B) G019.27+00.07	18:25:56.1	-12:04:47.2	26.2	2.4	2.7	2.2	+130,+300	250×230	7
(D) G028.53−00.25	18:44:17.4	-04:00:31.4	87.0	5.7	16.9	74.3	+200,+40	330×360	4
(E) G028.67+00.13	18:43:08.1	-03:44.54.3	79.5	5.1	11.5	28.7	+110,+380	180×160	9
(I) G038.95−00.47	19:04:08.1	+05:09:15.0	41.6	2.7	3.7	2.7	−120,+190	180×180	6
(J) G053.11+00.05	19:29:16.7	+17:54:40.0	22.0	1.8	0.8	0.2	+190,−10	160×170	5

[a] Butler & Tan (2009). [b] Rathborne et al. (2006). [c] Butler & Tan (2012). [d] Mass estimated by Kainulainen & Tan (2013) from combined Mid and Near IR extinction maps.

- Result
  - SiOのnarrow,broad emissionを両方検出

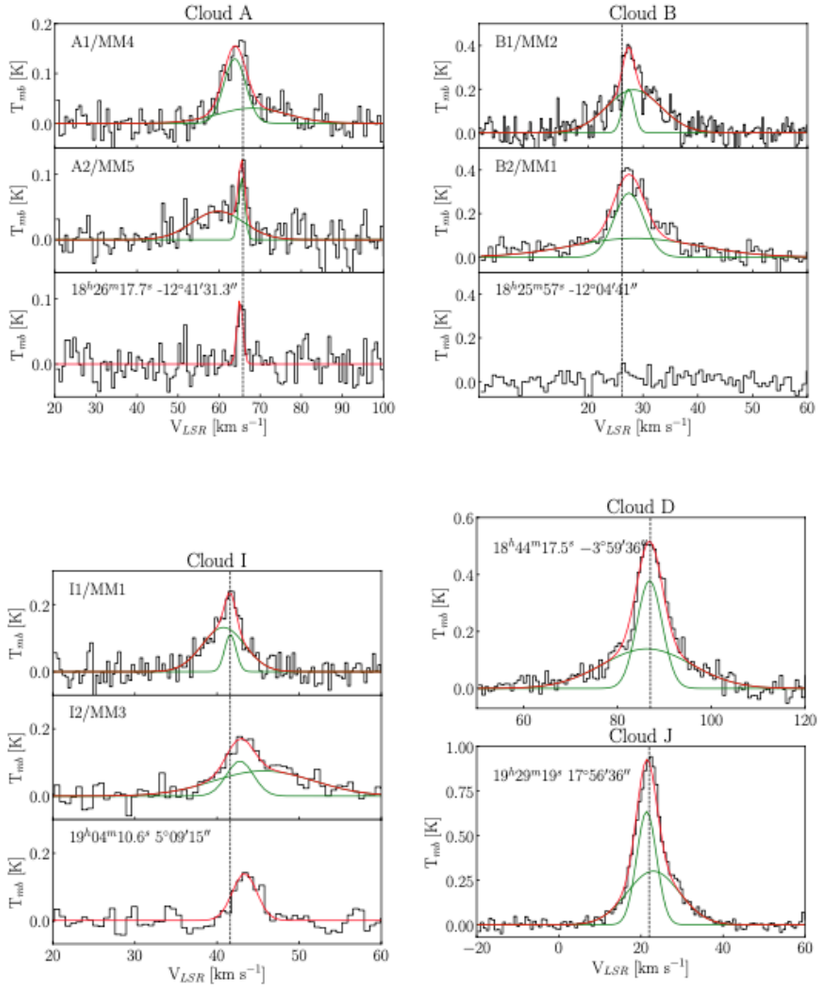

Figure 1. SiO spectra extracted toward selected positions (indicated in each panel) across cloud A (top left), B (top right), I (bottom left), D and J (bottom right) across a beam aperture of 30″. In all panels, the multi-Gaussian fitting is indicated as a red line, while the single Gaussian components are indicated as green lines. For all clouds, the corresponding central velocity is indicated as a vertical dashed line.

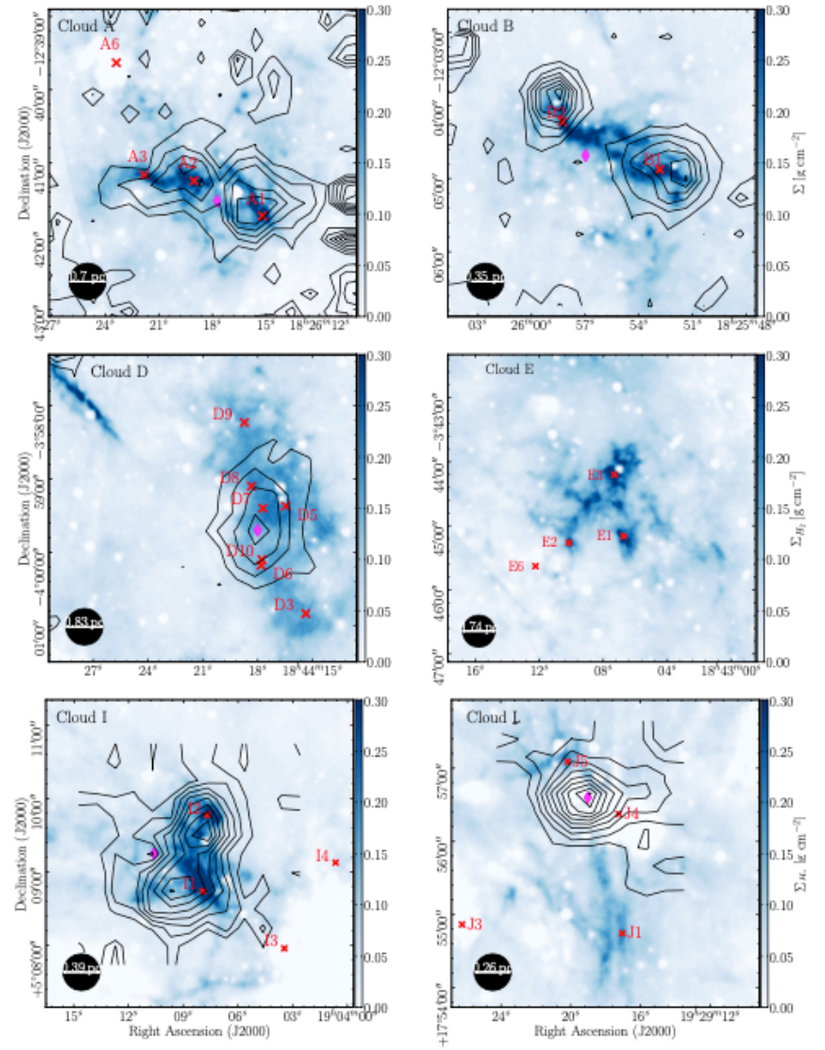

Figure 2. SiO(2-1) integrated intensity maps towards clouds A (top left panel), B (top right panel), and D (middle left panel), E (middle right panel), I (bott left panel) and J (bottom right panel). Emission levels (black contours) are from 3σ to 30σ by step of 6σ for cloud J and by steps of 3σ for all the ot IRDCs. The contours are superimposed on the mass surface density maps (grey scale) obtained by Kainulainen & Tan (2013). The integration ranges are 4 100 km s^{-1}, 5 to 45 km s^{-1}, 4 to 120 km s^{-1}, 10 to 70 km s^{-1} and −10 to 60 km s^{-1} for cloud A, B, D, I and J respectively. σ = 0.1 K km s^{-1} for cloud A and I, σ=0.2 K km s^{-1} for cloud B and J and σ = 0.5 K km s^{-1} for cloud D. The core positions (black crosses; Butler & Tan 2009, 2012) and the beam si (black circles) are shown in all panels.

- Result
  - narrow成分とbroad成分の分布

Narrow　　Broad

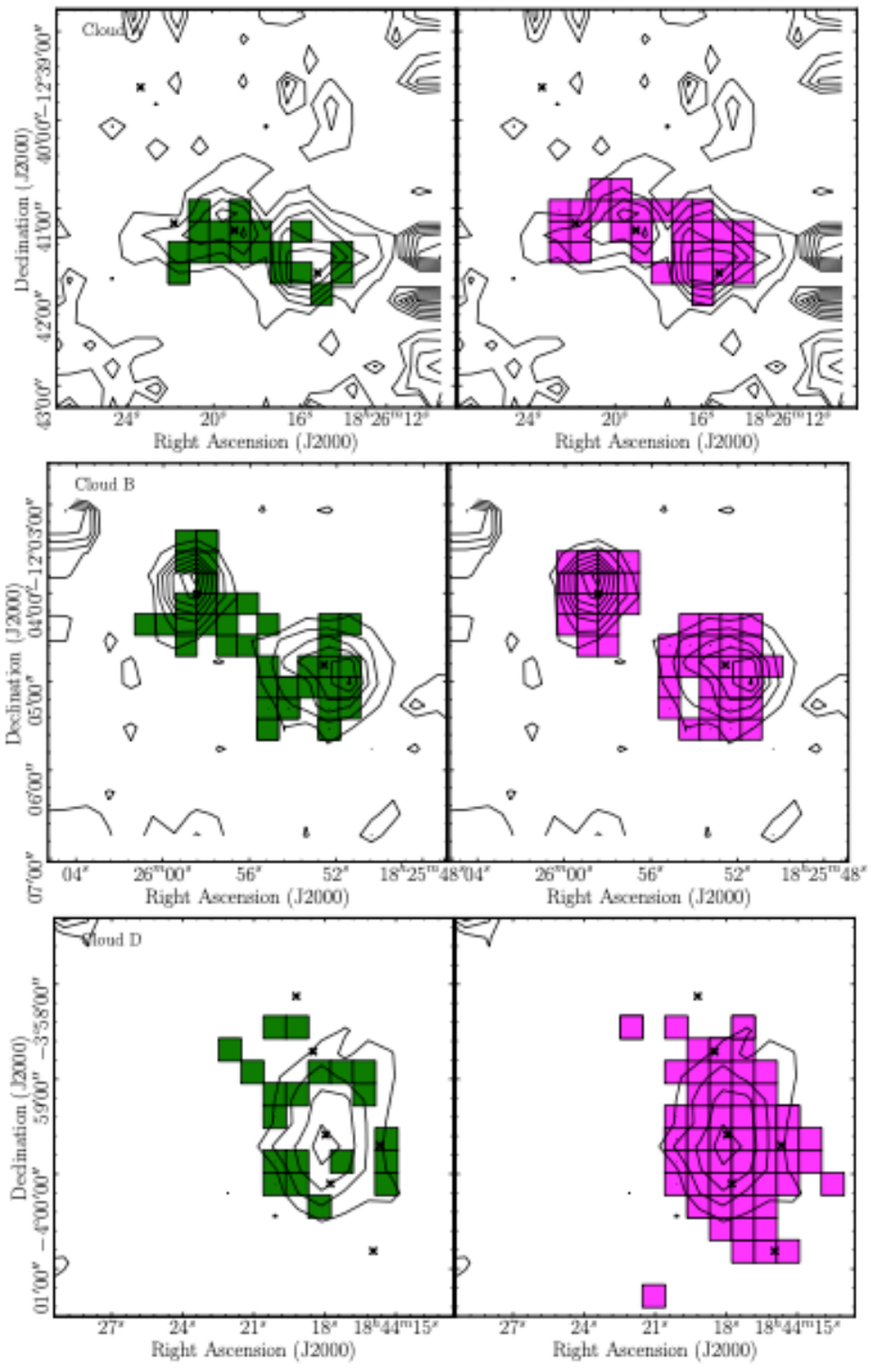

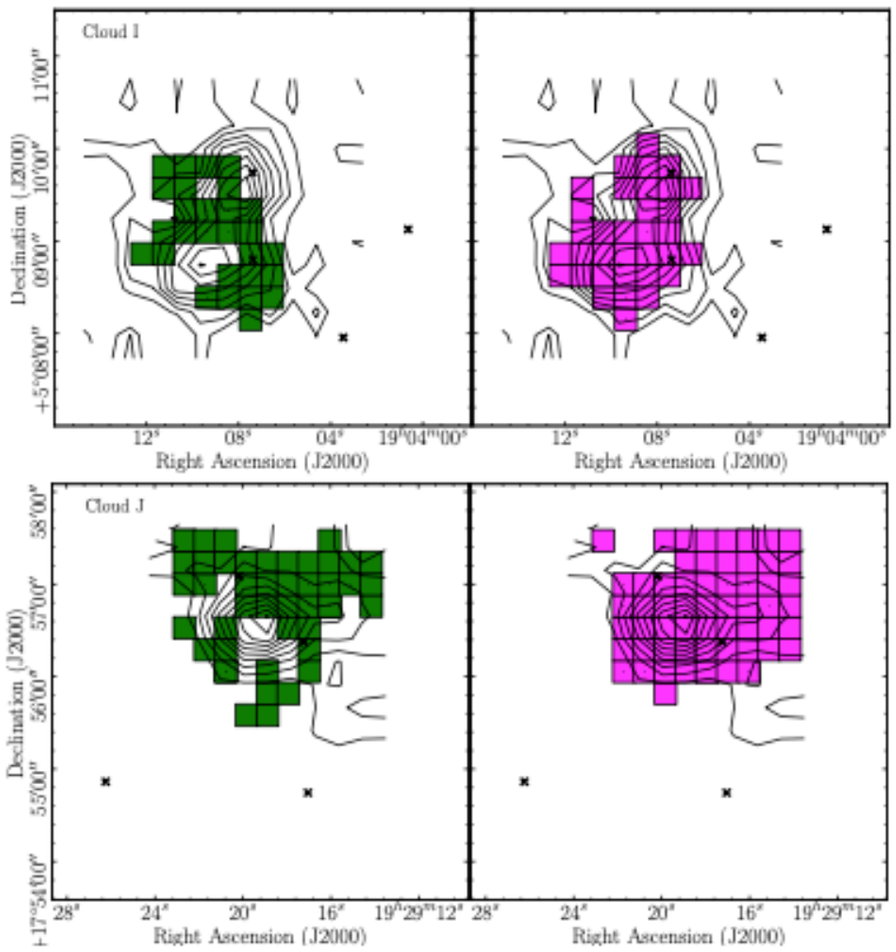

Figure 4. Spatial distributions of the narrow (green squares, left-hand panels) and broad (magenta squares, right-hand panels) SiO line width components toward cloud A, B and D from top to bottom respectively. Black contours corresponds to SiO integrated intensity maps as presented in Figure 2. Black crosses indicated the massive cores positions as in Butler & Tan (2012).

- Cloud B, D, J ではSiOは塊状の構造を持ち, narrow成分とbroad成分の空間分布は似ている（coexistしている）
  - → IRDC内部で進行中の星生成活動に付随するガス
- Cloud A, IではSiOはフィラメント状の構造を持ち, narrow成分とbroad成分の空間分布は異なる
  (中心速度も異なる)

- Result
  - Cloud A, J はGalactic Bubbleの近くに位置している

    → Cloud A, Jで検出されたnarrowかつ広がったSiO成分はIRDCと expanding shellによって押し出された分子雲との相互作用（衝突）をトレースしている

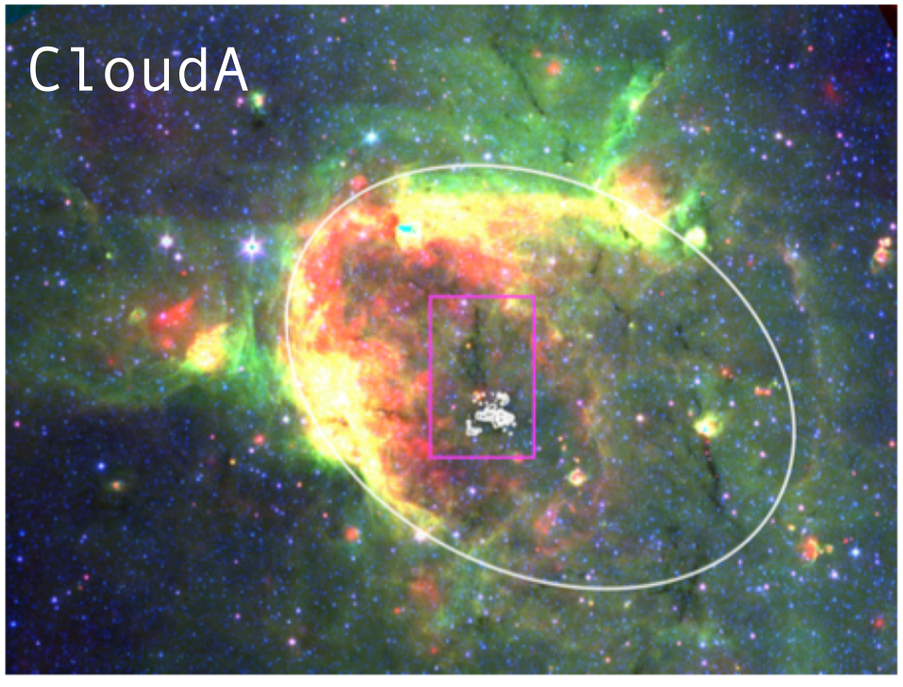

Figure 8. Three-color image of the Galactic Infrared Bubble N24 obtained from *Spitzer* data. The 4.5 μm and 8μm emission have been obtained from the GLIMPSE Survey (Benjamin et al. 2003, Churchwell et al. 2009) and are displayed in blue and green, respectively. The 24 μm emission is shown in red and has been obtained from the MIPSGAL Survey (Carey et al. 2009). The white ellipse roughly indicates the position of N24, while the magenta rectangle highlights the position of cloud A. White contours show the SiO integrated emission levels as in Figure 2.

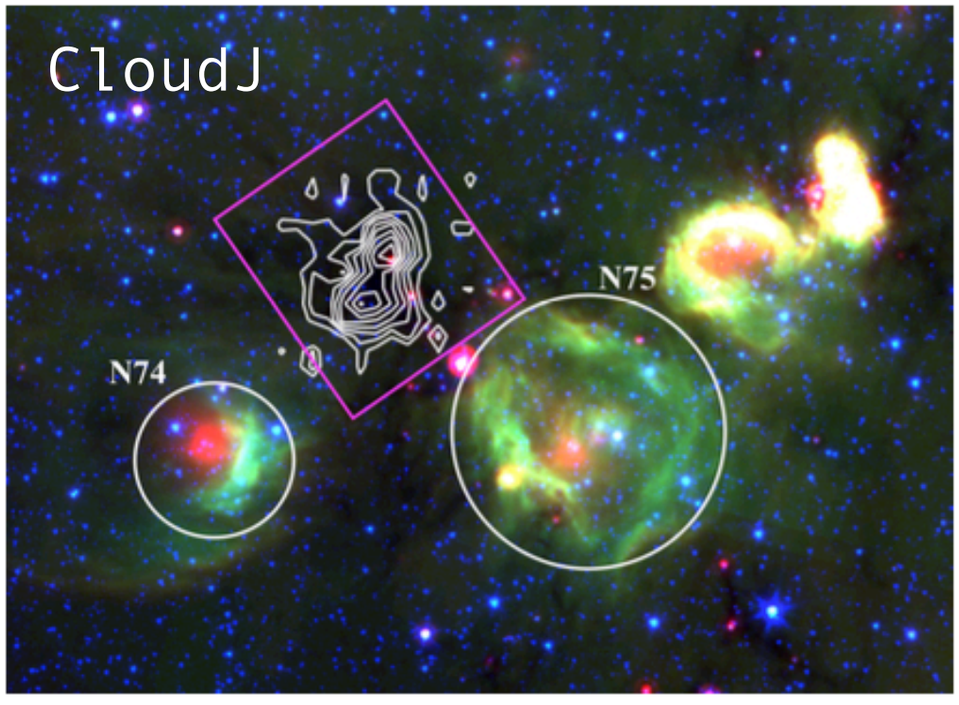

Figure 9. Three-color image of cloud I as surrounded by the two HII regions N74 and N75 (white circles). The 4.5 μm and 8μm emission have been obtained from the GLIMPSE Survey (Benjamin et al. 2003, Churchwell et al. 2009) and are displayed in blue and green respectively. The 24 μm emission is shown in red and has been obtained from the MIPSGAL Survey (Carey et al. 2009). The magenta rectangle indicates the position of cloud I. White contours show the SiO integrated emission levels as in Figure 2

1. Gravitoviscous Protoplanetary Disks with a Dust Component. IV. Disc Outer Edges, Spectral Indices, and Opacity Gaps

Vitaly Akimkin et al. Accepted by MNRAS https://arxiv.org/pdf/2010.06566

ABSTRACT

The crucial initial step in planet formation is the agglomeration of micron-sized dust into macroscopic aggregates. This phase is likely to happen very early during the protostellar disc formation, which is characterised by active gas dynamics. We present numerical simulations of protostellar/protoplanetary disc long-term evolution, which includes gas dynamics with self-gravity in the thin-disc limit, and bidisperse dust grain evolution due to coagulation, fragmentation, and drift through the gas. We show that the decrease of the grain size to the disc periphery leads to sharp outer edges in dust millimetre emission, which are explained by a drop in dust opacity coefficient rather than by dust surface density variations. These visible outer edges are at the location where average grain size $\approx \lambda/2\pi$, where λ is the observational wavelength, so discs typically look more compact at longer wavelengths if dust size decreases outwards. This allows a simple recipe for reconstructing grain sizes in disc outer regions. Discs may look larger at longer wavelengths if grain size does not reach $\lambda/2\pi$ for some wavelength. Disc visible sizes evolve non-monotonically over the first million years and differ from dust and gas physical sizes by factor of a few. We compare our model with recent observation data on gas and dust disc sizes, far-infrared fluxes and spectral indices of protoplanetary discs in Lupus. We also show that non-monotonic variations of the grain size in radial direction can cause wavelength-dependent opacity gaps, which are not associated with any physical gaps in the dust density distribution.

Key words: dust, extinction – hydrodynamics – opacity – protoplanetary discs – stars: pre-main-sequence – submillimetre: planetary systems

2. Hints for icy pebble migration feeding an oxygen-rich chemistry in the inner planet-forming region of disks

Andrea Banzatti et al. Accepted by ApJ https://arxiv.org/pdf/2009.13525

ABSTRACT

We present a synergic study of protoplanetary disks to investigate links between inner disk gas molecules and the large-scale migration of solid pebbles. The sample includes 63 disks where two types of measurements are available: *i)* spatially-resolved disk images revealing the radial distribution of disk pebbles (mm-cm dust grains), from millimeter observations with ALMA or the SMA, and *ii)* infrared molecular emission spectra as observed with *Spitzer*. The line flux ratios of H_2O with HCN, C_2H_2, and CO_2 all anti-correlate with the dust disk radius R_{dust}, expanding previous results found by Najita et al. (2013) for HCN/H_2O and the dust disk mass. By normalization with the dependence on accretion luminosity common to all molecules, only the H_2O luminosity maintains a detectable anti-correlation with disk radius, suggesting that the strongest underlying relation is between H_2O and R_{dust}. If R_{dust} is set by large-scale pebble drift, and if molecular luminosities trace the elemental budgets of inner disk warm gas, these results can be naturally explained with scenarios where the inner disk chemistry is fed by sublimation of oxygen-rich icy pebbles migrating inward from the outer disk. Anti-correlations are also detected between all molecular luminosities and the infrared index n_{13-30}, which is sensitive to the presence and size of an inner disk dust cavity. Overall, these relations suggest a physical interconnection between dust and gas evolution both locally and across disk scales. We discuss fundamental predictions to test this interpretation and study the interplay between pebble drift, inner disk depletion, and the chemistry of planet-forming material.

Keywords: circumstellar matter — protoplanetary disks — stars: pre-main sequence —

3. Gravity and rotation drag the magnetic field in high-mass star formation

S. Feng et al. Accepted by ApJ https://www2.mpia-hd.mpg.de/homes/beuther/beuther2020b.pdf

ABSTRACT

The formation of hot stars out of the cold interstellar medium lies at the heart of astrophysical research. Understanding the importance of magnetic fields during star formation remains a major challenge. With the advent of the Atacama Large Millimeter Array, the potential to study magnetic fields by polarization observations has tremendously progressed. However, the major question remains how much magnetic fields shape the star formation process or whether gravity is largely dominating. Here, we show that for the high-mass star-forming region G327.3 the magnetic field morphology appears to be dominantly shaped by the gravitational contraction of the central massive gas core where the star formation proceeds. We find that in the outer parts of the region, the magnetic field is directed toward the gravitational center of the region. Filamentary structures feeding the central core exhibit U-shaped magnetic field morphologies directed toward the gravitational center as well, again showing the gravitational drag toward the center. The inner part then shows rotational signatures, potentially associated with an embedded disk, and there the magnetic field morphology appears to be rotationally dominated. Hence, our results demonstrate that for this region gravity and rotation are dominating the dynamics and shaping the magnetic field morphology.

Keywords: Unified Astronomy Thesaurus concepts: Collapsing clouds (267), Dynamical evolution (421), Interstellar dynamics (839), Interstellar megnetic fields (845), Interstellar medium (847), Star formation (1569)

4. Observation of the Onset of Complex Organic Molecule Formation in Interstellar Ices

Laurie E. U. Chu et al. Accepted by ApJ https://arxiv.org/pdf/2010.05917

ABSTRACT

Isolated dense molecular cores are investigated to study the onset of complex organic molecule formation in interstellar ice. Sampling three cores with ongoing formation of low-mass stars (B59, B335, and L483) and one starless core (L694-2) we sample lines of sight to nine background stars and five young stellar objects (YSOs; $A_K \sim 0.5$ - 4.7). Spectra of these stars from 2-5 μm with NASA's Infrared Telescope Facility (IRTF) simultaneously display signatures from the cores of H_2O (3.0 μm), CH_3OH (C-H stretching mode, 3.53 μm) and CO (4.67 μm) ices. The CO ice is traced by nine stars in which five show a long wavelength wing due to a mixture of CO with polar ice (CO_r), presumably CH_3OH. Two of these sight lines also show independent detections of CH_3OH . For these we find the ratio of the CH_3OH:CO_r is 0.55±0.06 and 0.73±0.07 from L483 and L694-2, respectively. The detections of both CO and CH_3OH for the first time through lines of sight toward background stars observationally constrains the conversion of CO into CH_3OH ice. Along the lines of sight most of the CO exists in the gas phase and ≤15% of the CO is frozen out. However, CH_3OH ice is abundant with respect to CO (∼ 50%) and exists mainly as a CH_3OH-rich CO ice layer. Only a small fraction of the lines of sight contains CH_3OH ice, presumably that with the highest density. The high conversion of CO to CH_3OH can explain the abundances of CH_3OH ice found in later stage Class 1 low mass YSO envelopes (CH_3OH:CO_r ∼0.5-0.6). For high mass YSOs and one Class 0 YSO this ratio varies significantly implying local variations can affect the ice formation. The large CH_3OH ice abundance indicates that the formation of complex organic molecules is likely during the pre-stellar phase in cold environments without higher energy particle interactions (e.g. cosmic rays).

5. SiO emission as a probe of Cloud-Cloud Collisions in Infrared Dark Clouds

G. Consentino et al. Accepted by MNRAS https://arxiv.org/pdf/2009.13890

ABSTRACT

Infrared Dark Clouds (IRDCs) are very dense and highly extincted regions that host the initial conditions of star and stellar cluster formation. It is crucial to study the kinematics and molecular content of IRDCs to test their formation mechanism and ultimately characterise these initial conditions. We have obtained high-sensitivity Silicon Monoxide, SiO(2-1), emission maps toward the six IRDCs, G018.82−00.28, G019.27+00.07, G028.53−00.25, G028.67+00.13, G038.95−00.47 and G053.11+00.05 (cloud A, B, D, E, I and J, respectively), using the 30-m antenna at the Instituto de Radioastronomía Millimétrica (IRAM30m). We have investigated the SiO spatial distribution and kinematic structure across the six clouds to look for signatures of cloud-cloud collision events that may have formed the IRDCs and triggered star formation within them. Toward clouds A, B, D, I and J we detect spatially compact SiO emission with broad line profiles which are spatially coincident with massive cores. Toward the IRDCs A and I, we report an additional SiO component that shows narrow line profiles and that is widespread across quiescent regions. Finally, we do not detect any significant SiO emission toward cloud E. We suggest that the broad and compact SiO emission detected toward the clouds is likely associated with ongoing star formation activity within the IRDCs. However, the additional narrow and widespread SiO emission detected toward cloud A and I may have originated from the collision between the IRDCs and flows of molecular gas pushed toward the clouds by nearby HII regions.

Key words: ISM: clouds; ISM: individual objects: G018.82−00.28, G019.27+00.07, G028.53−00.25, G028.67+00.13, G038.95−00.47, G053.11+00.05; ISM: molecules; ISM: HII regions; ISM: kinematics and dynamics.

6. Chemical evolution during the formation of a protoplanetary disk

A. Coutens et al. Accepted by A&A http://arxiv.org/pdf/2010.05108

ABSTRACT

Context. The chemical composition of protoplanetary disks is expected to impact the composition of the forming planets. Characterizing the diversity of chemical composition in disks and the physicochemical factors that lead to this diversity is consequently of high interest.

Aims. The aim of this study is to investigate the chemical evolution from the prestellar phase to the formation of the disk, and to determine the impact that the chemical composition of the cold and dense core has on the final composition of the disk.

Methods. We performed 3D nonideal magneto-hydrodynamic (MHD) simulations of a dense core collapse using the adaptive-mesh-refinement RAMSES code. For each particle ending in the young rotationally supported disk, we ran chemical simulations with the three-phase gas-grain chemistry code Nautilus. Two different sets of initial abundances, which are characteristic of cold cores, were considered. The final distributions of the abundances of common species were compared to each other, as well as with the initial abundances of the cold core.

Results. We find that the spatial distributions of molecules reflect their sensitivity to the temperature distribution. The main carriers of the chemical elements in the disk are usually the same as the ones in the cold core, except for the S-bearing species, where HS is replaced by H_2S_3, and the P-bearing species, where atomic P leads to the formation of PO, PN, HCP, and CP. However, the abundances of less abundant species change over time. This is especially the case for "large" complex organic molecules (COMs) such as CH_3CHO, CH_3NH_2, CH_3OCH_3, and $HCOOCH_3$ which see their abundances significantly increase during the collapse. These COMs often present similar abundances in the disk despite significantly different abundances in the cold core. In contrast, the abundances of many radicals decrease with time. A significant number of species still show the same abundances in the cold core and the disk, which indicates efficient formation of these molecules in the cold core. This includes H_2O, H_2CO, HNCO, and "small" COMs such as CH_3OH, CH_3CN, and NH_2CHO. We computed the MHD resistivities within the disk for the full gas–grain chemical evolution and find results in qualitative agreement with the literature assuming simpler chemical networks.

Conclusions. In conclusion, the chemical content of prestellar cores is expected to affect the chemical composition of disks. The impact is more or less important depending on the type of species. Users of stand-alone chemical models of disks should pay special attention to the initial abundances they choose.

Key words. astrochemistry – stars: formation – stars: protostars – ISM: molecules

7. Time-Variable Radio Recombination Line Emission in W49A

C. G. DePree et al. Accepted by AJ http://arXiv.org/pdf/2010.04656

ABSTRACT

We present new Jansky Very Large Array (VLA) images of the central region of the W49A star-forming region at 3.6 cm and at 7 mm at resolutions of 0.″15 (1650 au) and 0.″04 (440 au), respectively. The 3.6 cm data reveal new morphological detail in the ultracompact H II region population, as well as several previously unknown and unresolved sources. In particular, source A shows elongated, edge-brightened, bipolar lobes, indicative of a collimated outflow, and source E is resolved into three spherical components. We also present VLA observations of radio recombination lines at 3.6 cm and 7 mm, and IRAM Northern Extended Millimeter Array (NOEMA) observations at 1.2 mm. Three of the smallest ultracompact H II regions (sources A, B2 and G2) all show broad kinematic linewidths, with $\Delta V_{FWHM} \gtrsim 40$ km s^{-1}. A multi-line analysis indicates that broad linewidths remain after correcting for pressure broadening effects, suggesting the presence of supersonic flows. Substantial changes in linewidth over the 21 year time baseline at both 3.6 cm and 7 mm are found for source G2. At 3.6 cm, the linewidth of G2 changed from 31.7±1.8 km s^{-1} to 55.6±2.7 km s^{-1}, an increase of +23.9±3.4 km s^{-1}. The G2 source was previously reported to have shown a 3.6 cm continuum flux density decrease of 40% between 1994 and 2015. This source sits near the center of a very young bipolar outflow whose variability may have produced these changes.

Keywords: HII regions- ISM: individual(W49A) - ISM: kinematics and dynamics-techniques: interferometric